Society For Biomaterials

Winner of the Young Investigator Award of the Society for Biomaterials at the 10th World Biomaterials Congress, May 17–22, 2016, Montreal QC, Canada

Microribbon-based hydrogels accelerate stem cell-based bone regeneration in a mouse critical-size cranial defect model

Li-Hsin Han,[1] Bogdan Conrad,[2] Michael T. Chung,[3] Lorenzo Deveza,[1] Xinyi Jiang,[1] Andrew Wang,[4] Manish J. Butte,[4] Michael T. Longaker,[5] Derrick Wan,[3] Fan Yang[1,6]

[1]Department of Orthopaedic Surgery, Stanford University School of Medicine, 300 Pasteur Dr, Edward Building Room 114, Stanford, California 94305
[2]Program of Stem Cell Biology and Regenerative Medicine, Stanford University, 300 Pasteur Dr, Edward Building Room 114, Stanford, California 94305
[3]Division of Plastic and Reconstructive Surgery, Stanford University School of Medicine, 257 Campus Dr, Hagey Building Room GK106, Stanford, California 94305
[4]Department of Pediatrics, Stanford University School of Medicine, 300 Pasteur Dr, Grant Building Room H307A, Stanford, California 94305
[5]Division of Plastic and Reconstructive Surgery, Institute for Stem Cell Biology and Regenerative Medicine, Stanford University School of Medicine, 257 Campus Dr, Hagey Building Room GK106, Stanford, California 94305
[6]Department of Bioengineering, Stanford University, 300 Pasteur Dr, Edward Building Room 114, Stanford, California 94305

Received 19 September 2015; revised 23 February 2016; accepted 9 March 2016
Published online 9 April 2016 in Wiley Online Library (wileyonlinelibrary.com). DOI: 10.1002/jbm.a.35715

Abstract: Stem cell-based therapies hold great promise for enhancing tissue regeneration. However, the majority of cells die shortly after transplantation, which greatly diminishes the efficacy of stem cell-based therapies. Poor cell engraftment and survival remain a major bottleneck to fully exploiting the power of stem cells for regenerative medicine. Biomaterials such as hydrogels can serve as artificial matrices to protect cells during delivery and guide desirable cell fates. However, conventional hydrogels often lack macroporosity, which restricts cell proliferation and delays matrix deposition. Here we report the use of injectable, macroporous microribbon (μRB) hydrogels as stem cell carriers for bone repair, which supports direct cell encapsulation into a macroporous scaffold with rapid spreading. When transplanted in a critical-sized, mouse cranial defect model, μRB-based hydrogels significantly enhanced the survival of transplanted adipose-derived stromal cells (ADSCs) (81%) and enabled up to three-fold cell proliferation after 7 days. In contrast, conventional hydrogels only led to 27% cell survival, which continued to decrease over time. MicroCT imaging showed μRBs enhanced and accelerated mineralized bone repair compared to hydrogels (61% vs. 34% by week 6), and stem cells were required for bone repair to occur. These results suggest that paracrine signaling of transplanted stem cells are responsible for the observed bone repair, and enhancing cell survival and proliferation using μRBs further promoted the paracrine-signaling effects of ADSCs for stimulating endogenous bone repair. We envision μRB-based scaffolds can be broadly useful as a novel scaffold for enhancing stem cell survival and regeneration of other tissue types. © 2016 Wiley Periodicals, Inc. J Biomed Mater Res Part A: 104A: 1321–1331, 2016.

Key Words: macroporous, injectable, hydrogels, stem cells, bone

How to cite this article: Han L-H, Conrad B, Chung MT, Deveza L, Jiang X, Wang A, Butte MJ, Longaker MT, Wan D, Yang F. 2016. Microribbon-based hydrogels accelerate stem cell-based bone regeneration in a mouse critical-size cranial defect model. J Biomed Mater Res Part A 2016:104A:1321–1331.

INTRODUCTION

Large size bone defects affect millions of people and can be caused by trauma, disease, congenital malfunction, or tumor resection.[1] Bone autografts and allografts are common treatments that account for 1.3 million operations per year in the United States.[2] Despite their well-established efficacy and immune compatibility,[1] autografts are often challenged by limited autologous bone supply, donor-site morbidity, and

Additional Supporting Information may be found in the online version of this article.
Correspondence to: F. Yang; e-mail: fanyang@stanford.edu

chronic pain. Allografts are more abundantly available, but place the patient at higher risk of immune rejection and disease transmission. Stem cell-based therapy for bone repair has emerged in the last decade to help overcome these challenges.[3–9] Adult stem cells with osteogenic potential, such as bone marrow-derived mesenchymal stem cells (MSCs) or adipose-derived stromal cells (ADSCs), can be harvested from the patients with minimal invasiveness and expanded *in vitro* for repairing bony defects.[3,4] Pluripotent stem cells, including embryonic stem cells (ESCs) and induced pluripotent stem cells (iPSCs) have also been explored for bone repair.[5,6] Stem cells may contribute to bone regeneration either directly via osteogenic differentiation[7] or indirectly by paracrine signaling to stimulate endogenous bone healing.[8] However, the efficacy of stem cells alone for repairing bony defects is often limited due to poor cell survival and engraftment,[9] lack of structural support,[9] and inefficient nutrient supply.[10]

To enhance the efficacy of stem cell-based therapy for bone repair, extensive attempts have been made to develop tissue-engineering scaffolds as the carriers for transplanting stem cells.[11–13] Hydrogels are a class of scaffolds that have been widely used to aid tissue regeneration due to their injectability, tunable biochemical compositions, and ease of direct cell encapsulation for achieving uniform cell distribution.[11,12] However, most hydrogels lack macropores larger than the size of encapsulated cells, which is critical for bone-healing bioactivities including cell spreading, vascularization, and new tissue deposition.[13] Most hydrogels also lack the mechanical strength for engineering load-bearing tissues such as cartilage and bones.[14] Prefabricated macroporous scaffolds[15–20] such as silk-based scaffolds,[15] poly (lactic-*co*-glycolic acid) scaffolds,[16] collagen sponges,[17] and hydroxyapatite-based scaffolds[18] provide macroporosity and stronger mechanical strength and have been used for bone-tissue engineering. However, current fabrication of macroporous scaffolds often require nonbiocompatible conditions, such as chemical erosion[19] and phase separation.[20] As such, cells can only be seeded onto the prefabricated porous scaffolds, often leading to poor cell-seeding efficiency and non-uniform cell distributions.[21] Furthermore, unlike hydrogels, prefabricated macroporous scaffolds are not moldable or injectable to fit into a complex bone defect,[22] which may otherwise promote scaffold-bone contact and subsequent integration.

To overcome the above limitations, we recently developed microribbon (μRB)-like, crosslinkable elastomers as scaffold building blocks which can encapsulate cells in three dimensions (3D) while simultaneously forming a highly macroporous scaffold.[23] Our previous studies showed that μRBs facilitate uniform cell encapsulation, allow formation of 3D scaffolds with tunable macroporosity, and support rapid cell spreading and proliferation *in vitro*. Flatness of μRBs facilitated force absorption and allowed the scaffolds to sustain large cyclic strain without losing integrity, which made them particularly attractive for engineering load bearing tissues.[23] The goal of the current study was to evaluate the potential of μRB-based scaffolds for *in vivo* bone repair using a critical-sized, mouse cranial defect model. We hypothesized that μRB-based scaffolds would promote stem cell engraftment and survival after transplantation, and that scaffold macroporosity would enhance host tissue ingrowth and promote bone regeneration.

MATERIALS AND METHODS

Materials

Type A gelatin, methacrylic anhydride, L-lysine hydrochloride, glutaraldehyde, 2,4,6-trimethylbenzoyl chloride, dimethylphenylphosphonite were purchased from Sigma–Aldrich (St. Louis, MO). All materials were used as received.

Synthesizing gelatin microribbons (μRBs)

Type A gelatin (GelA) was stirred in dimethyl sulfoxide (15 wt %) at 60 rpm and 50°C for 12 h to form a viscous solution, transferred into a 20-mL syringe pump, and ejected at 5 mL per h at room temperature into a tank of ethanol (3.5 L), which was located 1.8 m under the syringe; the tank was stirred at 1100 rpm. In ethanol, the stream of GelA was partially dried and turned into microfibers, which were further dried with acetone for 3 h to form μRBs. As-formed μRBs were chopped into short segments (<3 mm) in ethanol using a homogenizer. To enable photocrosslinking, μRBs were stirred at 25°C for 3 h in methacrylic anhydride (15 wt % in 100 mL methanol). The methacrylated μRBs were pre-fixed with glutaraldehyde (0.1% in 200 mL methanol) under vigorous stirring at 25°C for 3 h, washed three times with deionized water, and neutralized for 12 h in L-lysine hydrochloride (1% in 200 mL phosphate-buffered saline (PBS)). These μRBs were washed eight times with deionized water, freeze-dried, and stored at −20°C before use.

Needle injection of μRBs

μRBs were rehydrated in PBS by 7.5 wt % density, incubated at 37°C for 1 h, and transferred into a 1 mL syringe by the plunger side. The μRBs were injected through a 16-gauge needle into scaffold molds, under a roughly 3 mL min^{-1} ejection rate. The ejection was recorded using a digital camera. A video showing the injection is uploaded to the journal website.

Synthesizing hydrogel precursor: Methacrylated gelatin

To introduce methacrylate groups, GelA (10 g) was dissolved in 100 mL PBS under 50°C, and methacrylic anhydride (20 mL) was added by drops under constant stirring at 1000 rpm. The reaction continued for 2 h at 50°C. Crude product of methacrylated gelatin (GelMA) was extracted by dripping the solution into acetone (3 L), which precipitated GelMA and removed excessive methacrylic anhydride and by products. GelMA was purified by dialysis in deionized water, freeze-dried, and stored at −20°C before use.

Synthesizing photoinitiator lithium phenyl-2,4,6-trimethylbenzoylphosphinate

At room temperature and under argon, 2,4,6-trimethylbenzoyl chloride (3.2 g) was added dropwise to dimethylphenylphosphonite (3.0 g) under vigorous agitation.[24] The mixture was stirred at room temperature for 18 h, then heated to 50°C and mixed with excess lithium bromide (6.1 g) in 2-butanone (100 mL). After 10 min, the product was cooled to room temperature, allowed to rest for 4 h, and washed three times with

2-butanone to remove unreacted lithium bromide. Excess solvent was removed by vacuum.

Isolation and culture of adipose-derived stromal cells (ADSCs)

Mouse ADSCs were collected by harvesting inguinal fat pads isolated from 5- to 6-week-old, luciferase-positive/GFP-positive transgenic mice (supplied by the laboratory of Dr. Joseph Wu, Stanford University). All procedures involving animals were approved by the Stanford Institutional Review Board and NIH guidelines for the care and use of laboratory animals (NIH Publication #85–23 Rev. 1985) have been observed. Fat tissues were washed with PBS and digested at 37°C for 30 min with Blendzyme 3 (0.5 U mL^{-1}; Roche Diagnostics, Indianapolis, IN). Enzyme activity was neutralized with Dulbecco's Modified Eagle Medium containing 10% fetal bovine serum (Invitrogen, Carlsbad, CA) and 1% penicillin/streptomycin solution. The cells were then filtered through a 70-μm cell strainer to remove cellular debris, counted by using a hemocytometer, and seeded into tissue-culture flasks. Following an initial 48 h of incubation at 37°C and 5% CO_2, cells were washed with PBS and expanded in Dulbecco's Modified Eagle Medium with 10% fetal bovine serum, 1% penicillin/streptomycin, and 10 ng mL^{-1} basic fibroblast growth factor (PeproTech, Rocky Hill, NJ). Cells were passaged upon 85–90% confluence and second-passage cells were used for all experiments.

Formation of macroporous scaffolds from μRBs

Freeze-dried μRBs were rehydrated in PBS containing 0.05% photoinitiator to reach a μRB density of 150 mg mL^{-1}. Following 1 h of incubation at 37°C, the precursor was sandwiched between two glass slides (with a gap of 0.25 mm) and exposed to ultraviolet light (365 nm, 2 mW cm^{-2}) for 4 min. This exposure photocrosslinked the μRBs to produce a macroporous scaffold. For cell encapsulation, trypsinized ADSCs were gently mixed with the μRB precursor to reach a cell density of 10 million cells/mL prior to photocrosslinking. After 24 h of incubation (37°C, 5% CO_2), cell-laden scaffolds were cut into circular samples (4 mm in diameter) and transferred to 24-well plates before further use.

Formation of hydrogel scaffolds

GelMA were rehydrated in PBS containing 0.05% photoinitiator to reach a GelMA density of 150 mg mL^{-1}. Trypsinized ADSCs were mixed with the hydrogel precursor to reach a cell density of 10 million cells/mL prior to photocrosslinking. The precursor with ADSCs was sandwiched between two glass slides (with a gap of 0.25 mm) and exposed to ultraviolet light (365 nm, 2 mW cm^{-2}) for 4 min, forming hydrogel scaffolds. After 24 h of incubation (37°C, 5% CO_2), cell-laden scaffolds were cut into circular samples (4 mm in diameter) and transferred to 24-well plates before further use.

To prepare cryo-sectioning samples, μRB-based or hydrogel-based scaffolds were rinsed twice in 37°C PBS, fixed in 4% paraformaldehyde for 2 h, permeabilized by 0.5% Triton-X 100 (Sigma–Aldrich, St. Louis, MO) in PBS for 30 min, soaked in 60 wt % sucrose in PBS for 24 h, soaked in optimal cutting temperature (OCT) compound solution (VWR International, Radnor, PA) for 1 h, and frozen by liquid nitrogen vapor in imbedding molds. 8 μm-thick slides were prepared by cryosectioning the OCT-imbedded samples, and were stored at 5°C before use. To visualize cell morphology, the slides were stained for actin cytoskeletons using fluorescently labeled phalloidin (Sigma–Aldrich, St. Louis, MO) at 1:100 dilution, counter-stained for cell nuclei using Hoechst 33342 stain (Thermo Scientific, Waltham, MA) at 1:500 dilution and imaged using confocal microscopy (SP5, Leica, Buffalo Grove, IL) with oil-immersion lenses, 20× magnification, and 0.7 μm scanning resolution.

Animal surgery

Animal surgeries were performed in accordance with Stanford University Animal Care and Use Committee guidelines. NIH guidlines for the care and use of laboratory animals (NIH Publication #85–23 Rev. 1985) have been observed. CD-1 Foxn1 nude mice (Charles River Laboratories, Hollister, CA) were used for cranial defect procedures. Each treatment group contained at least four animals. The mice were deeply anesthetized by using an isoflurane vaporizer with 2.5% anesthetic dose. After removing the overlying pericranium, 4-mm cranial defects were created with a trephine drill on the contralateral left parietal bone with meticulous care to avoid damaging the underlying dura mater. The bone defects were treated with a 4-mm diameter μRB scaffold with ADSCs, hydrogel scaffolds with ADSCs, or either type of scaffold without cells. Mice with empty defects were prepared as a negative control.

Bioluminescence imaging

From day 0 to week 6 after defect generation and scaffold implantation, ADSC viability and implant location were monitored weekly via bioluminescence imaging. Mice were anesthetized with 2.5% isoflurane and injected subcutaneously under the scruff with 200 μL reporter probe D-luciferin (30 mg mL^{-1}). An IVIS Spectrum system (Caliper Life Sciences, Hopkinton, MA) was used to image the mice under 1.5% isoflurane anesthesia, at 60-s exposure time and 5 min acquisition period. Each mouse was imaged for photon radiance from the defect site, and was scanned until the peak signal was reached. Radiance was quantified in photons per second per centimeter squared per steradian.

X-ray microtomography

At weeks 0, 2, 4, and 6, the mineralization level of the implants was monitored via X-ray microtomography using a large-field Inveon PET-CT (Siemens, Washington, D.C.), with settings of 80 kVp X-ray voltage, 500 μA anode current, 80 μm voxel resolution, and 500 ms time for each 360° rotational step. The two-dimensional projection images were reconstructed into three-dimensional models with ImageJ (National Institutes of Health, Bethesda, MD). Voxels at the supraoccipital part of the occipital bone were used as the threshold to identify mineralized bone formation. Percentage healing in each mouse was determined by calculating the amount of reduction in the defect area.

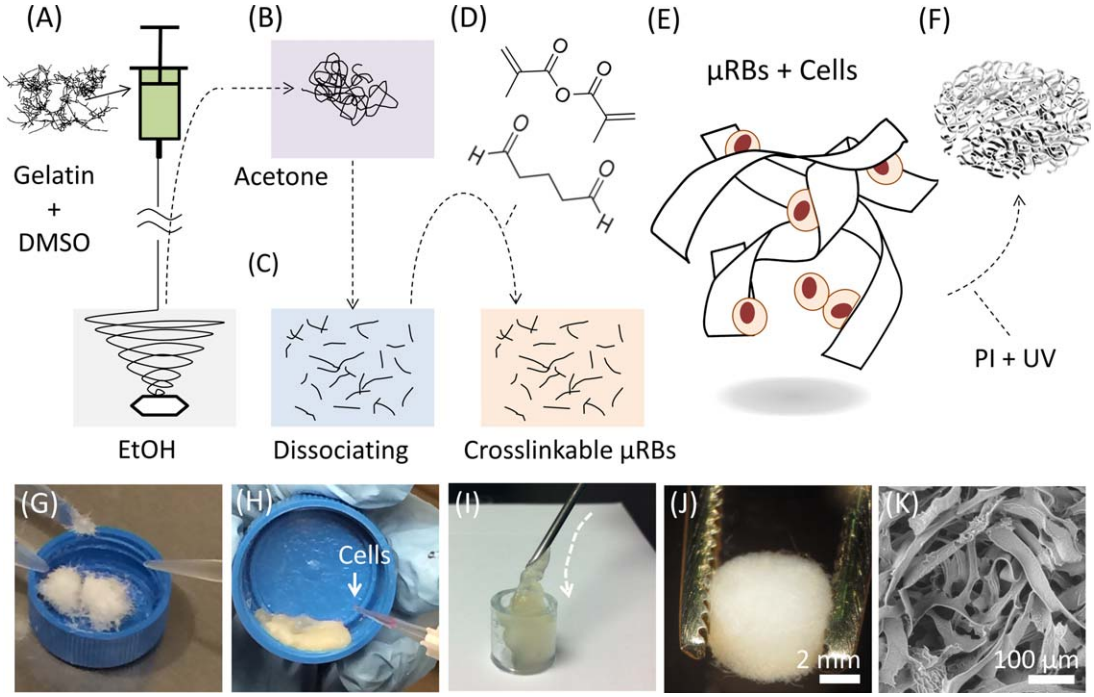

FIGURE 1. Fabrication scheme for a cell-laden, μRB-based scaffold. (A) Wet spinning. DMSO, dimethyl sulfoxide. (B) Acetone drying. (C, D) Dissociation, methacrylation, and aldehyde fixation. (E) Cell mixing. (F) Photocrosslinking with photoinitiator (PI) and ultraviolet light (UV). (G) Rehydrating μRBs. (H) Cell mixing. (I) Injection of cells and μRBs via syringe. (J) As-fabricated scaffold. (K) Scaffold macroporosity under scanning electron microscopy.

Histology and immunostaining

Mice were harvested at week 6 for histology. Tissue samples were fixed for 2 h in 4% paraformaldehyde, demineralized for 2 weeks in 16% ethylenediaminetetraacetic acid, and embedded in optimal cutting temperature compound before cryo-sectioning. Tissue morphology was examined with Masson trichrome staining (Thermo Scientific, Waltham, MA). For immunostaining, sectioned slices were treated with blocking buffer consisting of 2% goat serum and 3% bovine serum albumin in 1X PBS and incubated overnight at 4°C in rabbit polyclonal antibody against CD31 (1:100 dilution), osteocalcin (1:100 dilution), or green fluorescent protein (GFP) (1:100 dilution) (all from Abcam, Cambridge, MA). For secondary staining, sectioned slices were incubated for 1 h at room temperature with secondary antibodies: goat anti-rabbit horseradish peroxidase/3, 3′-diaminobenzidine for CD31/GFP (Abcam), and goat anti-rabbit Alexa Fluor 488 for osteocalcin (1:200 dilution) (Invitrogen, Carlsbad, CA). Nuclei were counterstained with Hoechst 33342 stain (Thermo Scientific, Waltham, MA) and images were taken with a Zeiss fluorescence microscope. Sections were stained with all reagents without primary antibody for negative controls.

Stiffness measurements via atomic force microscopy

The stiffness of μRB and hydrogel scaffolds was measured with a silicon nitride cantilever with 5.4-μm colloidal probe (AppNano), 0.03–0.08 N m^{-1} spring constant, and 4–6 kHz fundamental resonance frequency. All measurements were performed in warm PBS at 37°C using a MFP-3D system (Asylum Research). Stiffness maps of μRB/hydrogel (10 × 10 grid across the width of the ribbon) were measured in force-volume mode on three samples; each map yielded 100 force-distance curves recorded at a probing rate of 0.5 Hz. The stiffness value was calculated by fitting the loading part of each force-distance curve to the Hertz model, assuming a Poisson's ratio of 0.4 for the samples.

Statistical analysis

All data were expressed as mean ± standard error. Statistical significance was determined via analysis of variance using Student's t test with equal variance. p values (two-tailed) <0.05 were considered statistically significant, and p values <0.005 were considered statistically highly significant.

RESULTS

Gelatin μRBs form macroporous scaffolds via photocrosslinking

Photocrosslinkable μRBs were synthesized by wet-spinning as previously reported.[23] Gelatin dissolved in dimethyl sulfoxide was ejected from a syringe into stirred ethanol and precipitated to form microfibers [Fig. 1(A)]. The fibers were turned into 40–70 μm wide ribbons via acetone drying [Fig. 1(B)], dissociated, methacrylated, glutaraldehyde fixed, and freeze-dried for storage [Fig. 1(C,D)]. Prior to use, μRBs were rehydrated in phosphate-buffered saline and mixed with trypsinized mouse ADSCs [Fig. 1(G,H)]. The paste-like physical property of the rehydrated μRBs allows their

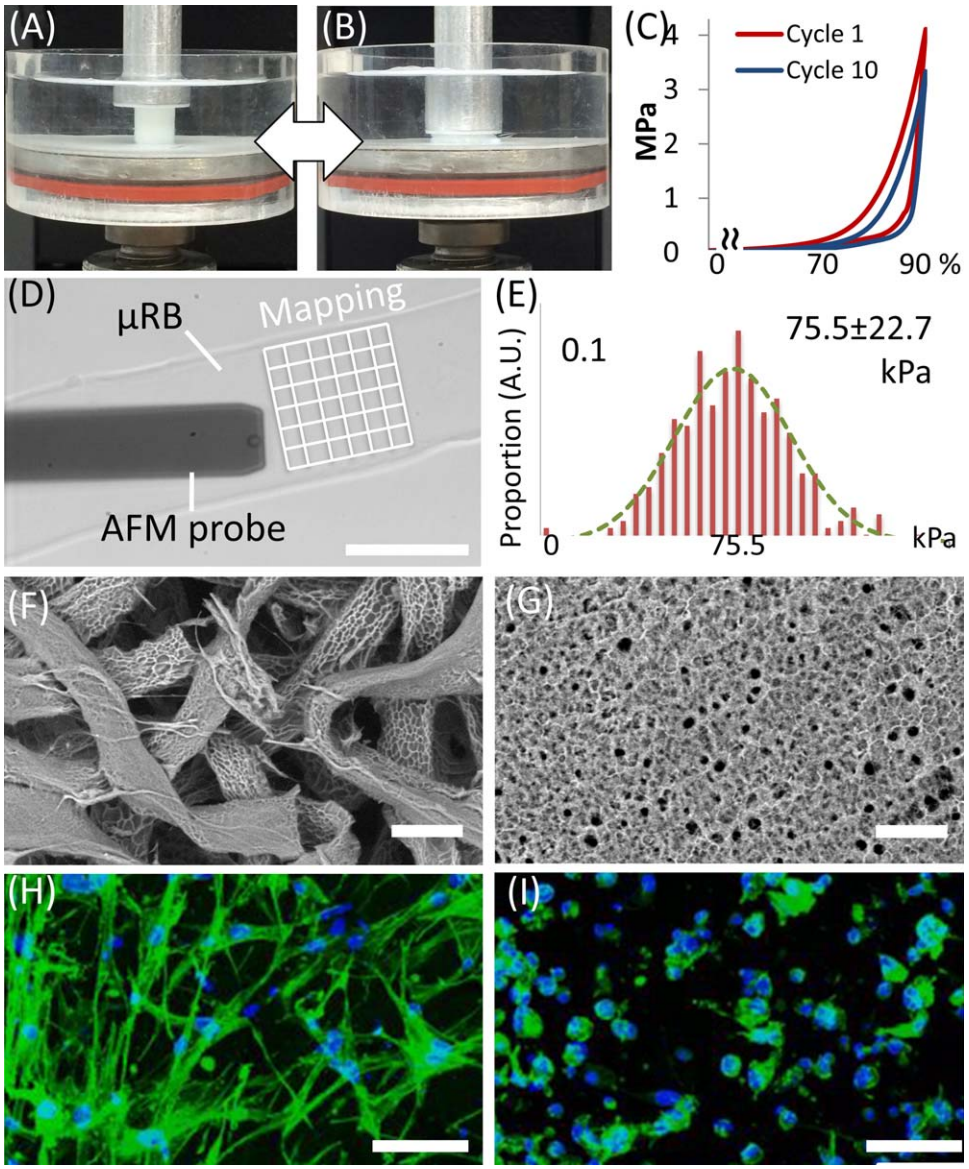

FIGURE 2. Physical properties of μRB-based scaffold. (A-B) μRB-based scaffold under 90% cyclic compression. (C) Stress–strain loops of μRB scaffolds show scaffolds maintained mechanical integrity upon cyclic compression, as indicated by overlapping loops. (D) Stiffness of individual μRB measured by atomic force microscopy (AFM). (E) Stiffness quantified by AFM measurement ($n = 300$). The stiffness of microribbon (75.5 ± 22.7 kPa, mean ± standard deviation) is within the range that reportedly promotes bone differentiation. (F, G) Scaffold porosity under variable-pressure SEM showed large macropores in the μRB scaffolds, and much smaller micropores in the conventional gelatin hydrogels. (H, I) Two days post-encapsulation, adipose-derived stem cells exhibited extensive spreading in μRB-based scaffolds (H), while remained mostly round in conventional gelatin hydrogels (I) (green: actin; blue: cell nuclei). Scale bars indicate 50 μm in (D) and (F–I).

injection into scaffold molding through needles of 16 G or larger size [Fig. 1(I) and Supporting Information Video]. To fabricate macroporous scaffolds, molded μRBs were photocrosslinked (365 nm, 4 min, 2.5 mW cm^{-2}) in the presence of a photoinitiator [Fig. 1(E–J)]. The resulting scaffolds were characterized by high mechanical flexibility [Fig. 2(A–C)] and highly interconnected macropores that provided abundant internal space and surface area [Fig. 1(K)]. All these features have been reported to promote osteogenic differentiation of stem cells and facilitate bone–matrix production.[13,25] To provide stiffness conditions reported to promote bone differentiation,[12,26] we modulated our aldehyde-fixation procedures to obtain μRBs with stiffness of 75.5 ± 22.7 kPa [300 point measurements across 3 microribbons; Fig. 2(D,E)]. Stiffness was measured with atomic force microscopy.[27]

To compare the efficacy of μRB-based scaffolds for bone repair with that of existing hydrogel platforms, we also fabricated hydrogels of methacrylated gelatin as control groups.[28] These hydrogels provided collagen-derived ligands that are similar to those displayed by the μRBs. To provide the similar matrix stiffness, the hydrogel scaffolds were fabricated with a stiffness of 65.1 ± 2.1 kPa using 15% (w/v) methacrylated gelatin as precursor.

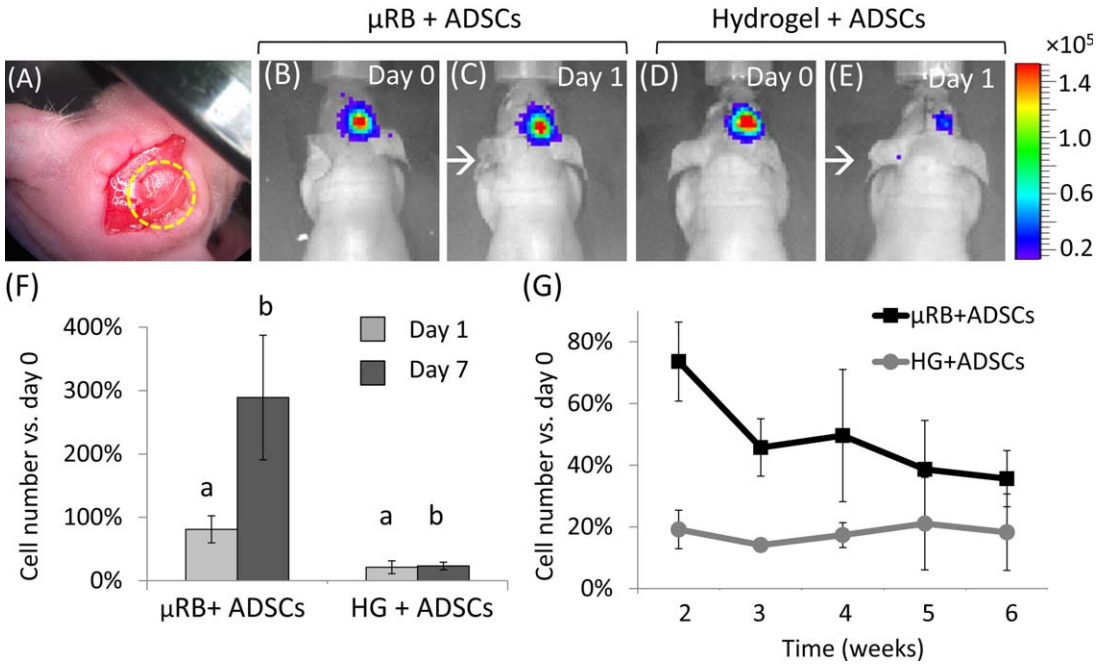

FIGURE 3. Bioluminescence imaging (BLI) showed μRB-based scaffolds enhanced stem cell survival and proliferation *in vivo* compared to conventional hydrogels after being transplanted in a mouse critical size cranial defect model. (A) Transplanted scaffolds in the cranial defect. (B–E) BLI on days 1 and 7. The red end of the color scale indicates higher signal (in radiance unit, p/sec/cm^3/sr). (F) BLI imaging showed μRB scaffolds led to significantly higher cell survival at day 1 than in conventional hydrogels ($p = 0.002$). μRBs enabled cell proliferation up to three-fold after 7 days, whereas the cell number in HG controls remained low; (G) μRB scaffolds led to consistently higher number of transplanted stem cells than conventional hydrogels throughout 6 weeks ($p < 0.05$), with the greatest difference observed within the first 2 weeks. $n = 4$ per group, error-bars: standard deviations.

μRB-based scaffolds promote cell spreading in 3D

To examine the effects of macroporosity on cell morphology in 3D, μRB or hydrogel-based precursors (both at 15% (w/v)) were mixed with ADSCs and photocrosslinked into 250-μm thick, sheet-form scaffolds. Cell-laden scaffolds were incubated in ADSC growth medium for 1 day before implantation or analyzed for cell morphology. Our μRB-based scaffolds enabled direct cell encapsulation, while forming macropores ranging from 150 to 300 μm [Fig. 2(F)], a range which was previously reported to facilitate bone-tissue formation *in vivo*.[25] In contrast, conventional gelatin hydrogels exhibited substantially smaller pore sizes (~20 μm) [Fig. 2(G)]. Confocal imaging 24 h after encapsulation revealed extensive spreading of ADSCs throughout the μRB-based scaffolds [Fig. 2(H) and Supporting Information Video], while ADSCs in the hydrogel-based scaffolds maintained a round morphology with minimal cell spreading [Fig. 2(I) and Supporting Information Video]. Such dramatic difference in cell morphology indicates the advantage of μRB-based scaffolds in supporting cell survival and proliferation, which are known to prefer extensive cell spreading.[29]

μRB-based scaffolds promote cell viability *in vivo*

Critical-sized cranial defects 4 mm in diameter (which do not heal endogenously in the absence of treatment) were created in athymic mice on the right parietal bones as described previously[30]; these defects were implanted with μRB- or hydrogel-based scaffolds harvested from the scaffold sheets [Fig. 3(A)]. Four implanted groups were prepared in total: mice with μRB or hydrogel scaffolds plus ADSCs (μRB + ADSC and hydrogel + ADSC groups), mice with either type of scaffold without cells (μRB-only and hydrogel-only groups), and mice with defects that were not implanted with anything (negative control).

Over 6-weeks post-surgery, ADSCs in μRB scaffolds showed significantly higher cell numbers (in percentages relative to day 0) than ADSCs in hydrogel scaffolds. The observed cell numbers were influenced by both cell survival and cell proliferation. On day 1, bioluminescence imaging (BLI) revealed 81.1% ± 21.3% ADSC survival in the μRB + ADSC group, but significantly decreased cell survival (26.6% ± 10.1%) in the hydrogel + ADSC group ($p < 0.002$) [Fig. 3(B–F)]. At week 1, the μRB + ADSC group displayed substantial ADSC proliferation (289.2% ± 98.2% vs. day 0, $p = 0.002$ vs. day 1), while the hydrogel + ADSC group presented roughly unchanged cell numbers (23.3% ± 5.9% vs. day 0, $p > 0.5$ vs. day 1) [Fig. 3(G)]. From weeks 2 to 6, both groups experienced gradually decreased cell viability, while the ADSCs in μRB scaffolds maintained twice as much viability as those in hydrogel scaffolds ($p < 0.05$) [Fig. 3(G)]. Because ADSCs in μRB and hydrogel scaffolds were exposed to similar biochemical ligands and matrix stiffness (75.5 ± 22.7 kPa vs. 65.1 ± 2.1 kPa), these BLI results indicated that the dramatically enhanced survival of ADSCs in μRB scaffolds stemmed from the high macroporosity in the μRB-based scaffolds, which was the main difference between the μRB + ADSC group and the hydrogel + ADSC group.

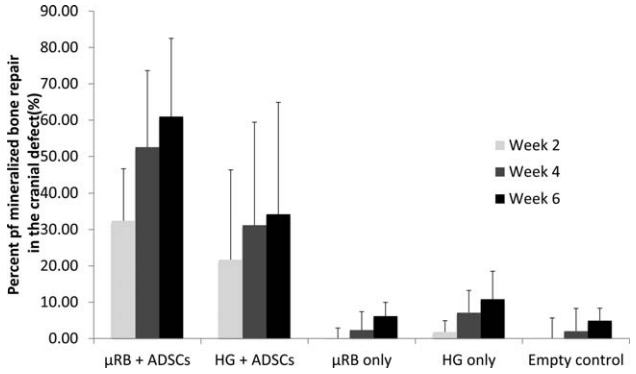

FIGURE 4. Analyzed microCT imaging data showed cell-laden μRBs led to faster and greater mineralized bone repair than conventional hydrogels in a critical sized mouse cranial defect over 6 weeks. Percent of bone healing was normalized to the defect size at day 1. $n = 4$ per group, error-bars: standard deviations.

μRB-based scaffolds with ADSCs promote bone healing, bone-scaffold integration, and vascularization

X-ray microtomography (micro-CT) and histology were used to investigate how scaffold types and ADSC transplantation influence bone healing. The effects of scaffold type were studied with μRB-based and hydrogel-based implants, and the efficacy of ADSC incorporation was elucidated with cell-laden and acellular implants. Results from empty defects provided a point of reference. To exclude other variables that could affect bone repair, the ADSCs were cultured in growth medium without osteogenic growth factors, and the scaffolds were fabricated without osteoconductive cues such as hydroxyapatite coating[31] or osteogenic growth factors such as bone morphogenetic protein.[32]

Both the μRBs and HGs seeded with ADSCs led to noticeable mineralized bone formation as early as week 2 ($32\% \pm 14\%$ in μRB vs. $21\% \pm 23\%$ in HG), with higher variability across samples in the HG group (Fig. 4). Compared to HG with ADSCs, μRB with ADSCs led to 52% more mineralized bone in week 2, and this trend continued to increase over time (Fig. 4). By 6 weeks, μRB with ADSCs led to 79% more mineralized bone repair than HG with ADSCs (Fig. 4). While the difference is not statistically significant due to the high variability in the HG + ADSC group, there is a clear trend that cell seeded μRBs led to faster and greater mineralized bone formation than cell seeded HG. For both μRBs and HGs, new mineralized bone formation was the greatest within the first 4 weeks, and slowed down afterwards (Fig. 4). In contrast to the cell-laden scaffolds, negligible bone filling ($<5\%$) was observed in defects with scaffolds alone without cells and in defects without implants (Figs. 4 and 5). Because μRB and HG scaffolds provided similar stiffness and biochemical cues, the micro-CT results indicate that the observed faster bone filling stemmed from the macroporosity of the μRB-based scaffolds. Furthermore, the dramatic difference between the cell-laden groups and the acellular groups demonstrates that transplanted ADSCs play an essential role in bone regeneration.

Trichrome staining showed extensive collagen-rich tissue ingrowth in defects implanted with μRB scaffolds harboring ADSCs, both at the center and at the edges of the defect [Fig. 5(F,K,P)]. In defects implanted with μRB scaffolds without ADSCs, tissue ingrowth was observed, but with lower collagen content [Fig. 5(HMR)]. Collagen-rich tissues appeared in defects implanted with hydrogel scaffolds with ADSCs [Fig. 5(G,L,Q)]. In defects implanted with hydrogel scaffolds without ADSCs, tissue ingrowth was absent; instead, fibrous capsules formed around the hydrogel scaffolds [Fig. 5(I,N,S)]. In terms of implant integrity, μRB scaffolds with or without ADSCs exhibited well-preserved macroporous structures, whereas hydrogel scaffolds with or without ADSCs were mostly degraded and disappeared after 42 days post-implantation.

Vascularization is essential for bone healing.[33] Here, immunostaining against cluster of differentiation 31 (CD31), an endothelial cell marker, revealed signs of angiogenesis throughout defects implanted with μRB scaffolds with or without ADSCs; the macropores resembled interconnected "tunnels" for vascular-tissue expansion [Fig. 6(A,C)]. Vascularization was much more limited in defects implanted with hydrogel scaffolds with ADSCs [Fig. 6(B)]. Signs of angiogenesis were absent in defects without scaffolds and in defects implanted with hydrogel scaffolds without ADSCs [Fig. 6(D,E)]. CD31 staining showed that both μRB macroporosity and transplanted ADSCs promote implant vascularization. The enhanced vascularization of the μRB + ADSC group may also support the viability of ADSCs via increased nutrient supply.

ADSCs stimulate endogenous bone regeneration via paracrine signaling

To elucidate how ADSCs participate in bone regeneration (via osteogenic differentiation or via paracrine signaling), we immunostained defects for osteocalcin, a pro-osteoblastic molecule. This staining revealed extensive osteogenesis throughout defects implanted with μRB scaffolds with ADSCs [Fig. 6(F)]. Osteogenesis was detected in defects with hydrogel scaffolds with ADSCs, but was limited due to hydrogel collapse [Fig. 6(G)]. Osteogenesis was negligible in empty defects [Fig. 6(E,J)] and in defects implanted with either scaffold without ADSCs [Fig. 6(H,I)]. These observations are consistent with our micro-CT results [Fig. 5(A–E)], which showed that bone healing occurred most rapidly in defects implanted with μRB scaffolds with ADSCs, occurred more slowly in defects implanted with hydrogel scaffolds with ADSCs, and was absent from the defects lacking scaffolds or ADSCs.

Because our ADSCs were harvested from mice expressing green fluorescent protein (GFP), we used GFP expression to track ADSC fate in the cranial defects. A few transplanted ADSCs were detected at the center and the periphery of defect filled with μRB scaffolds [Fig. 6(F)], but not near the hydrogel scaffolds [Fig. 6(G)]. In both groups, new bone formation was mostly contributed by endogenous cells, which did not express GFP. Thus, the observed bone healing [Fig. 5(A,B)] was mainly due to bone formation by host cells that were stimulated by transplanted ADSCs via paracrine signaling.

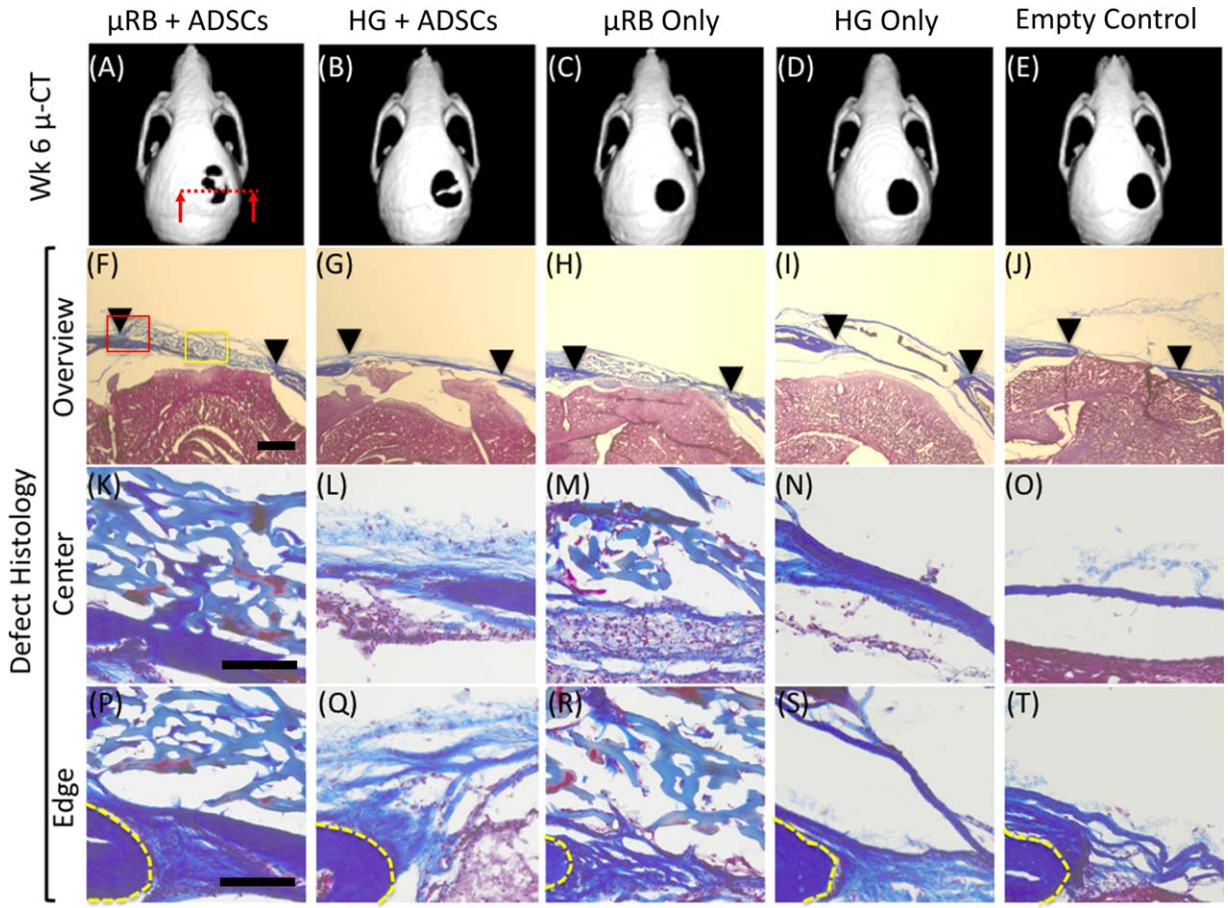

FIGURE 5. Representative micro-CT images and histological cross sections of mouse cranial defects at 6 weeks after treatment with μRB-based scaffolds or conventional hydrogels, with or without adipose-derived stem cells. Untreated cranial defects were included as controls. (A–E) Representative micro-CT images indicate only stem cell-seeded scaffolds led to mineralized bone formation in the critical size cranial defects, with ADSC+μRB group showing the highest degree of mineralized bone deposition. (F–T) Masson's Trichrome stain of collagen at cranial defect sites at week 6 after transplantation. The images display a cross-section of the skull, and connective tissue is stained blue. Representative images with higher resolutions of locations of images in F–J are shown in I–T. (F–J) Low magnification views of entire cranial defect region. Arrows: edges of cranial defects. (K–O) High magnification views of central region within the cranial defects, as indicated by yellow box in F. (P–T) High magnification views of interface between implants and the original cranial defects, as indicated by red box in F. Yellow line: edge of original cranial defects. Scale bars: 500 μm in (F–J); 100 μm in (K–T).

DISCUSSION

Healing of large bony defects represents a significant challenge clinically, as traditional autografts or allografts are subject to drawbacks that include donor-site complications, insufficient donor tissue supply, and the risk of immune rejection and disease transmission. Stem cell-based therapies augment native bone healing with osteogenic bioactivities, such as osteogenic differentiation and paracrine signaling stimulation.[7,8] These bioactivities are most effective when the transplanted stem cells are supported physically and biochemically to facilitate cell engraftment, cell proliferation, nutrient supply, and bone-tissue deposition.[10,34]

Here, we approached such goals by developing microporous scaffolds using photocrosslinkable μRBs as building blocks. *In vivo* transplantation of ADSCs in μRB-based scaffolds dramatically enhanced ADSC engraftment, survival, and proliferation [Fig. 2(B–G)]. The macroporosity formed among μRBs promoted endogenous tissue integration [Fig. 5(K,P)], vascularization [Fig. 6(A)], and mineralized bone formation [Fig. 5(A)]. In comparison with conventional grafting materials such as hydrogels and prefabricated macroporous scaffolds, this novel biomaterial possesses several important advantages, which are described below.

Promotion of cell spreading, survival, and proliferation

Low cell viability is a common challenge for stem cell-based therapies, and is often due to a lack of cell adhesion and spreading after transplantation.[10,34] In contrast, integrin-mediated cell attachment and the resultant signaling cascades are known to rescue cells from apoptosis,[29] stimulated DNA synthesis, and promoted cell survival and growth.[35] Nutrient supply also plays an important role in sustaining stem-cell survival.[10] In our μRB-based scaffolds, cell adhesion is supported by the gelatin-based ligands of the μRBs, while nutrient diffusion and cell spreading are promoted by the macropores [Fig. 2(H) and Supporting Information Video]. Macropore-supported vascularization [Fig. 6(A,C)] may also promote long-term cell survival. In addition to the beneficial effects on bone repair, such

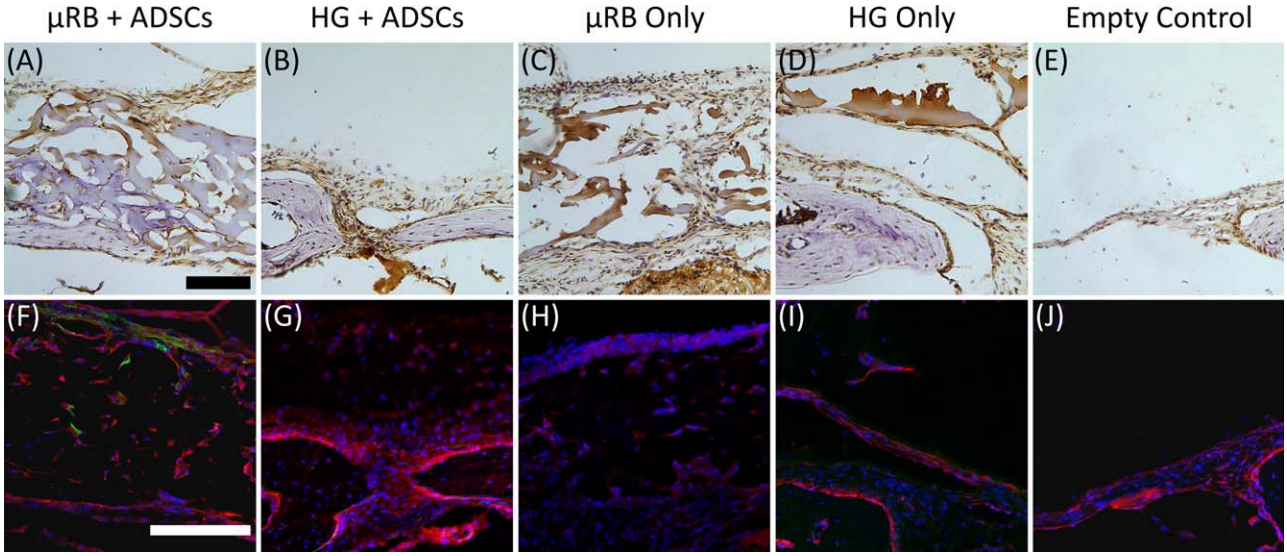

FIGURE 6. Representative staining of CD-31 (for endothelial cells) and osteocalcin (for bone) in cranial defects at 6 weeks *in vivo*. (A–E) CD31-positive cells (brown) counter-stained with Harris's hematoxylin (purple). (F–J) Immunofluorescence staining of osteocalcin (red) counter-stained by transplanted ADSCs (green) and cell nuclei (blue). At 6-week time point, transplanted ADSCs were only detectable in groups treated with μRB + ADSCs. Most regenerated bone tissues were contributed by endogenous bone regeneration. Scale bars, 100 μm.

enhancement of cell viability is promising for a broad variety of cell-based therapies, such as the stem cell regeneration of fat,[36] cartilage,[37] or blood vessels.[38]

Tunability of macropore formation

Unlike μRB-based scaffolds, most conventional hydrogels lack macropores that are bigger than cells [Fig. 2(G)], therefore restricting cell proliferation, migration, and new tissue deposition. Here, transplanting ADSCs to cranial defects with methacrylated gelatin hydrogels instead of μRBs caused significantly lower cell viability [Fig. 3(F,G)], limited vascularization [Fig. 6(A,C)], and slower bone formation [Fig. 5(A,B)]. Efforts have been made to overcome such limitations. Improvements in hydrogel porosity are often achieved by lowering the hydrogel's polymer concentration.[39] Enzyme-cleavable hydrogels allow cell-mediated matrix degradation,[40] while biocompatible porogens have been embedded and dissolved in hydrogels to produce macropores.[41] Nonetheless, these methods often simultaneously degrade scaffold integrity and the hydrogel's biochemical composition, complicating the control of scaffold properties. In contrast, our macroporous scaffolds are generated in one step by crosslinking the μRBs as building blocks [Fig. 1(G–K)]. As a result, scaffold macroporosity is determined only by μRB packing density [Fig. 2(F)], while matrix stiffness [Fig. 2(D,E)] and the biochemical properties that cells sense from the scaffold are determined separately by the properties of individual μRBs [Fig. 1(D)]. This building block-based approach will simplify the future design of macroporous scaffolds for bone repair and for other types of tissue regeneration.

Direct cell encapsulation and injectability

Conventional macroporous scaffolds are mostly prefabricated, and incorporating cells into them requires external cell seeding, which is prone to inefficient cell distribution[21] and may become problematic for scaffolds with clinically relevant dimensions. In contrast, in the current strategy, μRBs are paste-like in phosphate-buffered saline and can be thoroughly mixed with cells before photocrosslinking [Fig. 1(H–K)]. The resulting cell distribution is highly uniform regardless of the level of porosity or scaffold dimensions [Fig. 2(H)]. Such direct cell encapsulation simplifies the control of cell density, which determines the efficiency of cell-to-cell communication and is known to directly influence bone-tissue regeneration.[42] Moreover, μRBs can be injected via syringe to fill irregular defects [Fig. 1(I) and Supporting Information Video), which is promising for minimally invasive surgeries[22] that aim for less surgical trauma, lower infection risk, and shorter patient recovery time.

Support for ADSC paracrine signaling for endogenous bone healing

Adipose tissues represent an abundant and readily accessible source of stem cells in our body.[3] ADSCs are known to stimulate wound healing by delivering paracrine-signaling factors that promote cell survival,[43] vascularization,[44] endogenous stem-cell recruitment, and the differentiation of stem cells along desirable lineages.[8,43,44] Results from our cranial defect model suggest that such paracrine signaling was primarily responsible for the observed bone healing [Fig. 5(A–E) versus Fig. 6(F–J)]. The relation between higher cell proliferation [Fig. 3(B,C)] and faster defect filling [Fig. 5(A,B)] in the μRB + ADSC group suggests that μRBs may further such paracrine-signaling effects by enhancing the proliferation and survival of ADSCs.

Our results also highlight the therapeutic potential of transplanting primary ADSCs with the μRB-based scaffolds. ADSCs without *ex vivo* manipulations, such as predifferentiation, may be incorporated through a point-of-care process,[45]

in which ADSCs are extracted as primary cells and transplanted with μRBs immediately upon isolation. This process aims to save time and resources by eliminating *ex vivo* cell manipulation, which may help increase the efficiency and cost-effectiveness of stem cell-based bone therapy.

Potential incorporation of osteoconductive reagents

The efficacy of μRBs for bone repair was evidenced by progressive bone formation in the cranial defects of mice that received μRBs and ADSCs [Fig. 5(A,F,K,P)]. However, it is worth noting that our μRB synthesis remains to be optimized. To evaluate the potential of using μRBs for stem cell-based bone repair, here we excluded the osteoconductive reagents and osteogenic growth factors that are commonly incorporated into bone-grafting biomaterials.[31,32] In future studies, our μRBs may be incorporated with these components to further accelerate bone regeneration.

Versatility

In addition to bone repair, our μRBs are highly versatile and can be recustomized for various types of tissue regeneration. For example, glycosaminoglycans may be introduced into the μRBs to promote the formation of cartilage tissue.[14] To enable crosslinking in dark environments, such as inside the body, the methacrylate groups may be replaced with molecules that can be crosslinked through other mechanisms, such as the thiol and maleimide-based ligands that crosslink each other via thiol-ene coupling.[11] μRB stiffness and packing density may be optimized for other wound-healing processes that are sensitive to matrix stiffness and porosity. Finally, μRBs may be embedded with drug-releasing vehicles, such as poly (lactic-*co*-glycolic acid) particles,[32] to deliver biomolecules for tissue repair, such as bone morphogenetic protein for osteogenesis,[32] TGF-β for chondrogenesis,[37] and vascular endothelial growth factor for vascularization.[38]

In summary, the challenges of stem cell-based therapies for large bone defects necessitate new strategies for cell transplantation. Here, we approach this goal by using photocrosslinkable μRBs as carriers for stem cell transplantation, which dramatically enhanced ADSC survival, accelerated defect vascularization and host tissue integration, and promoted the paracrine-signaling effects for endogenous bone healing. This μRB-based platform is highly versatile and can be customized for engineering a broad variety of tissues.

REFERENCES

1. Dinopoulos H, Dimitriou R, Giannoudis PV. Bone graft substitutes: What are the options? Surgeon 2012;10:230–239.
2. Betz RR. Limitations of autograft and allograft: New synthetic solutions. Orthopedics 2002;25:s561–s570.
3. Schäffler CB A. Concise review: Adipose tissue-derived stromal cells—Basic and clinical implications for novel cell-based therapies. Stem Cells 2007;5:818–827.
4. Song L, Tuan RS. Transdifferentiation potential of human mesenchymal stem cells derived from bone marrow. Faseb J 2004;18: 980–982.
5. Marolt D, Campos IM, Bhumiratana S, Koren A, Petridis P, Zhang G, Spitalnik PF, Grayson WL, Vunjak-Novakovic G. Engineering bone tissue from human embryonic stem cells. Proc Natl Acad Sci USA 2012;109:8705–8709.
6. Levi B, Hyun JS, Montoro DT, Lo DD, Chan CK, Hu S, Sun N, Lee M, Grova M, Connolly AJ, Wu JC, Gurtner GC, Weissman IL, Wan DC, Longaker MT. In vivo directed differentiation of pluripotent stem cells for skeletal regeneration. Proc Natl Acad Sci USA 2012; 109:20379–20384.
7. Shih YR, Hwang Y, Phadke A, Kang H, Hwang NS, Caro EJ, Nguyen S, Siu M, Theodorakis EA, Gianneschi NC, Vecchio KS, Chien S, Lee OK, Varghese S. Calcium phosphate-bearing matrices induce osteogenic differentiation of stem cells through adenosine signaling. Proc Natl Acad Sci USA 2014;111:990–995.
8. Lee K, Kim H, Kim JM, Kim JR, Kim KJ, Kim YJ, Park SI, Jeong JH, Moon YM, Lim HS, Bae DW, Kwon J, Ko CY, Kim HS, Shin HI, Jeong D. Systemic transplantation of human adipose-derived stem cells stimulates bone repair by promoting osteoblast and osteoclast function. J Cell Mol Med 2011;15:2082–2094.
9. Hidalgo-Bastida LA, Cartmell SH. Mesenchymal stem cells, osteoblasts and extracellular matrix proteins: Enhancing cell adhesion and differentiation for bone tissue engineering. Tissue Eng B Rev 2010;16:405–412.
10. Yeatts AB, Geibel EM, Fears FF, Fisher JP. Human mesenchymal stem cell position within scaffolds influences cell fate during dynamic culture. Biotechnol Bioeng 2012;109:2381–2391.
11. Deforest CA, Sims EA, Anseth KS. Peptide-functionalized click hydrogels with independently tunable mechanics and chemical functionality for 3D cell culture. Chem Mater 2010;22:4783–4790.
12. Nii M, Lai JH, Keeney M, Han LH, Behn A, Imanbayev G, Yang F. The effects of interactive mechanical and biochemical niche signaling on osteogenic differentiation of adipose-derived stem cells using combinatorial hydrogels. Acta Biomater 2013;9:5475–5483.
13. Hollister SJ. Porous scaffold design for tissue engineering. Nat Mater 2005;4:518–524.
14. Carter DR, Beaupre GS. Skeletal Tissue Regeneration. Skeletal Function and Form. Cambridge, UK: Cambridge University Press; 2001. p 161–200.
15. Mandal BB, Grinberg A, Gil ES, Panilaitis B, Kaplan DL. High-strength silk protein scaffolds for bone repair. Proc Natl Acad Sci USA 2012;109:7699–7704.
16. Thevenot PT, Nair AM, Shen J, Lotfi P, Ko CY, Tang L. The effect of incorporation of SDF-1alpha into PLGA scaffolds on stem cell recruitment and the inflammatory response. Biomaterials 2010;31: 3997–4008.
17. Nehrer S, Breinan HA, Ramappa A, Hsu HP, Minas T, Shortkroff S, Sledge CB, Yannas IV, Spector M. Chondrocyte-seeded collagen matrices implanted in a chondral defect in a canine model. Biomaterials 1998;19:2313–2328.
18. Fierz FC, Beckmann F, Huser M, Irsen SH, Leukers B, Witte F, Degistirici O, Andronache A, Thie M, Muller B. The morphology of anisotropic 3D-printed hydroxyapatite scaffolds. Biomaterials 2008;29:3799–3806.
19. Chen VJ, Ma PX. Nano-fibrous poly(l-lactic acid) scaffolds with interconnected spherical macropores. Biomaterials 2004;25:2065–2073.
20. Ji C, Khademhosseini A, Dehghani F. Enhancing cell penetration and proliferation in chitosan hydrogels for tissue engineering applications. Biomaterials 2011;32:9719–9729.
21. Melchels FPW, Tonnarelli B, Olivares AL, Martin I, Lacroix D, Feijen J, Wendt DJ, Grijpma DW. The influence of the scaffold design on the distribution of adhering cells after perfusion cell seeding. Biomaterials 2011;32:2878–2884.
22. Kretlow JD, Young S, Klouda L, Wong M, Mikos AG. Injectable biomaterials for regenerating complex craniofacial tissues. Adv Mater 2009;21:3368–3393.
23. Han L-H, Yu S, Wang T, Behn AW, Yang F. Microribbon-like elastomers for fabricating macroporous and highly flexible scaffolds that support cell proliferation in 3D. Adv Funct Mater 2013;23:346–358.
24. Fairbanks BD, Schwartz MP, Bowman CN, Anseth KS. Photoinitiated polymerization of PEG-diacrylate with lithium phenyl-2,4,6-trimethylbenzoylphosphinate: Polymerization rate and cytocompatibility. Biomaterials 2009;30:6702–6707.
25. Murphy CM, Haugh MG, O'Brien FJ. The effect of mean pore size on cell attachment, proliferation and migration in collagen-glycosaminoglycan scaffolds for bone tissue engineering. Biomaterials 2010;31:461–466.

26. Adam J, Engler SS, Lee Sweeney H, Discher Dennis E. Matrix elasticity directs stem cell lineage specification. Cell 2006;126: 677–689.
27. Sun N, Yazawa M, Liu J, Han L, Sanchez-Freire V, Abilez OJ, Navarrete EG, Hu S, Wang L, Lee A, Pavlovic A, Lin S, Chen R, Hajjar RJ, Snyder MP, Dolmetsch RE, Butte MJ, Ashley EA, Longaker MT, Robbins RC, Wu JC. Patient-specific induced pluripotent stem cells as a model for familial dilated cardiomyopathy. Sci Transl Med 2012;4:130ra47.
28. Nichol JW, Koshy ST, Bae H, Hwang CM, Yamanlar S, Khademhosseini A. Cell-laden microengineered gelatin methacrylate hydrogels. Biomaterials 2010;31:5536–5544.
29. Frisch SM, Screaton RA. Anoikis mechanisms. Curr Opin Cell Biol 2001;13:555–562.
30. Behr B, Sorkin M, Lehnhardt M, Renda A, Longaker MT, Quarto N. A comparative analysis of the osteogenic effects of BMP-2, FGF-2, and VEGFA in a calvarial defect model. Tissue Eng Part A 2012;18:1079–1086.
31. Phipps MC, Clem WC, Grunda JM, Clines GA, Bellis SL. Increasing the pore sizes of bone-mimetic electrospun scaffolds comprised of polycaprolactone, collagen I and hydroxyapatite to enhance cell infiltration. Biomaterials 2012;33:524–534.
32. Ji Y, Xu GP, Zhang ZP, Xia JJ, Yan JL, Pan SH. BMP-2/PLGA delayed-release microspheres composite graft, selection of bone particulate diameters, and prevention of aseptic inflammation for bone tissue engineering. Ann Biomed Eng 2010;38:632–639.
33. Nguyen LH, Annabi N, Nikkhah M, Bae H, Binan L, Park S, Kang Y, Yang Y, Khademhosseini A. Vascularized bone tissue engineering: Approaches for potential improvement. Tissue Eng B Rev 2012;18:363–382.
34. Hyun JS, Tran MC, Wong VW, Chung MT, Lo DD, Montoro DT, Wan DC, Longaker MT. Enhancing stem cell survival in vivo for tissue repair. Biotechnol Adv 2013;31:736–743.
35. Maniotis AJ, Chen CS, Ingber DE. Demonstration of mechanical connections between integrins, cytoskeletal filaments, and nucleoplasm that stabilize nuclear structure. Proc Natl Acad Sci USA 1997;4:849–854.
36. Lequeux C, Oni G, Wong C, Damour O, Rohrich R, Mojallal A, Brown SA. Subcutaneous fat tissue engineering using autologous adipose-derived stem cells seeded onto a collagen scaffold. Plast Reconstr Surg 2012;130:1208–1217.
37. Sampat SR, O'Connell GD, Fong JV, Alegre-Aguaron E, Ateshian GA, Hung CT. Growth factor priming of synovium-derived stem cells for cartilage tissue engineering. Tissue Eng Part A 2011;17: 2259–2265.
38. Oliviero O, Ventre M, Netti PA. Functional porous hydrogels to study angiogenesis under the effect of controlled release of vascular endothelial growth factor. Acta Biomater 2012;8:3294–3301.
39. Bertz A, Wohl-Bruhn S, Miethe S, Tiersch B, Koetz J, Hust M, Bunjes H, Menzel H. Encapsulation of proteins in hydrogel carrier systems for controlled drug delivery: Influence of network structure and drug size on release rate. J Biotechnol 2013;163:243–249.
40. Benton JA, Fairbanks BD, Anseth KS. Characterization of valvular interstitial cell function in three dimensional matrix metalloproteinase degradable PEG hydrogels. Biomaterials 2009;30:6593–6603.
41. Han LH, Lai JH, Yu S, Yang F. Dynamic tissue engineering scaffolds with stimuli-responsive macroporosity formation. Biomaterials 2013;34:4251–4258.
42. Purpura KA, Aubin JE, Zandstra PW. Sustained in vitro expansion of bone progenitors is cell density dependent. Stem Cells 2004; 22:39–50.
43. Rehman J, Traktuev D, Li J, Merfeld-Clauss S, Temm-Grove CJ, Bovenkerk JE, Pell CL, Johnstone BH, Considine RV, March KL. Secretion of angiogenic and antiapoptotic factors by human adipose stromal cells. Circulation 2004;109:1292–1298.
44. Bhang SH, Cho SW, La WG, Lee TJ, Yang HS, Sun AY, Baek SH, Rhie JW, Kim BS. Angiogenesis in ischemic tissue produced by spheroid grafting of human adipose-derived stromal cells. Biomaterials 2011;32:2734–2747.
45. Mielczarek M, Ciecwierz D, Galaska R, Zielinski M, Taszner M, Gruchala M, Raczak G, Rynkiewicz A. Autologous transplantation of bone marrow stem cells prepared by the point-of-care system in a patient with myocardial ischemia due to coronary artery chronic total occlusion. Int J Cardiol 2013;168:e104–e105.